Random walk of antiferromagnetic skyrmions in granular films

K. Y. Jing [1], C. Wang [2,*] and X. R. Wang [1,3,†]

[1] *Physics Department, The Hong Kong University of Science and Technology (HKUST), Clear Water Bay, Kowloon, Hong Kong*

[2] *Center for Joint Quantum Studies and Department of Physics, School of Science, Tianjin University, Tianjin 300350, China*

[3] *HKUST Shenzhen Research Institute, Shenzhen 518057, China*

(Received 24 January 2021; revised 4 May 2021; accepted 11 May 2021; published 24 May 2021)

The impressive absence of the skyrmion Hall effect of antiferromagnetic (AFM) skyrmions in clean systems has raised high expectations of AFM skyrmions as information carriers and the potential applications in data storage technology. Here, we report an undesired behavior of current-driven AFM skyrmion dynamics in granular thin films. Understanding the motion of AFM skyrmions in disordered systems is crucial because disorders are inevitable in all materials. Micromagnetic simulations show that AFM skyrmions deviate from their trajectory in the clean limit. Interestingly, the transverse (to the current direction) motion is diffusive, i.e., the mean square of transverse displacement is proportional to the traveling time. The longitudinal (along with the current direction) motion is always hindered by disorders. An effective theory based on the stochastic Thiele equation can account for the observed phenomena. At a very strong disorder above a critical value that depends on the current density, AFM skyrmions are pinned. Our findings should be important for future spintronic devices based on AFM skyrmions.

DOI: 10.1103/PhysRevB.103.174430

I. INTRODUCTION

Magnetic skyrmions [1–4] are a strong candidate for future nonvolatile memory devices due to their small sizes, topological protection, and low driven currents [5–8]. Skyrmions, stabilized by the Dzyaloshinskii-Moriya interaction (DMI) [9,10], can appear in ferromagnets [11–16], ferrimagnets [17–19], and antiferromagnets [20–23]; in bulk compounds, surfaces, thin films, heterostructures, nanowires, and nanodots. Compared with their ferromagnetic counterpart, antiferromagnetic (AFM) skyrmions are more promising due to the absence of the skyrmion Hall effect [24,25], room-temperature stability [21], high-speed responses [26–29], and the absence of stray fields [30]. Motivated by these advantages, there is increasing interest in AFM materials [31,32] and AFM spintronics devices [33–36].

A good understanding of the current-driven AFM skyrmions dynamics in disordered materials is vital since impurities are inevitable in reality. The validity of those results from pervasive theoretical works for clean systems [26,37–39] (or with a single defect [40–42]) should be tested in the presence of disorders. Disorders have essential effects on the dynamics of many trivial and nontrivial topological magnetic textures such as domain walls [43,44], vortices [43,45], and ferromagnetic skyrmions [46–48]. The common wisdom is that disorders do not affect an AFM skyrmion's transverse motion because the transverse motion comes from the Magnus force that should be exactly canceled out due to the opposite forces on the two sublattices. However, disorder-induced force is not the same as the Magnus force that has a skyrmion number origin. A careful study of the transverse motion of AFM skyrmions in disordered films is needed.

In this paper, we model an AFM granular thin film by a Voronoi tessellation [see Fig. 1(a)]. We use micromagnetic simulations to study the AFM skyrmion propagation driven by spin-transfer torques. For weak disorders and strong driven currents, AFM skyrmions propagate along the current direction at constant averaged velocities, although disorders always slow down their speeds, and skyrmions in this regime are termed as the *hindering phase*. Meanwhile, disorder-generated random forces cause the skyrmions undergoing a Brownian motion in the transverse direction. This Brownian motion can also be viewed as an effective temperature that exerts a random field or force on an AFM skyrmion. A theory that shows the equivalence of the randomness in model parameters and the effective temperature is developed within the Thiele's approach [49]. The theory can account for both longitudinal and transverse skyrmion motions. At strong disorders and weak driven currents, AFM skyrmions are pinned where the concept of effective temperature is no longer valid. The critical disorder strength above which skyrmions are pinned and the phase diagram in the current-disorder plane are analytically obtained.

The paper is organized as follows. The model is presented in Sec. II. Our numerical results are given in Sec. III. Namely, there exists a critical disorder below (above) which an AFM skyrmion is in the hindering (pinning) phase and the transverse motion of the AFM skyrmion in the hindering phase is diffusive. Sections IV A and IV B discuss a theory that explains the skyrmion motion in the hindering phase and the critical disorder separating the hindering phase and the pinning phase. Section V concludes this work with some discussions.

*Corresponding author: physcwang@tju.edu.cn

†Corresponding author: phxwan@ust.hk

II. MODEL

Our granular AFM thin film of size $1024a\times256a\times a$ is a Hamiltonian on the square lattice in the xy plane similar to that used in Ref. [47], but for a ferromagnetic granular film,

$$\mathcal{H}_{\rm AFM} = \sum_{\langle ij\rangle} J_{ij}\boldsymbol{m}_i\cdot\boldsymbol{m}_j + \sum_{\langle ij\rangle}\boldsymbol{D}_{ij}\cdot(\boldsymbol{m}_i\times\boldsymbol{m}_j) - \sum_{\boldsymbol{I}}\sum_{\boldsymbol{i}\in\boldsymbol{I}} K_{\boldsymbol{I}}(\boldsymbol{m}_i\cdot\hat{z})^2 + \mathcal{H}_{\rm DDI}, \quad (1)$$

where $\boldsymbol{m_i}$ is the unit direction of the magnetization at site $\boldsymbol{i} = (x_i, y_i)$, $a = 1$ nm is the lattice constant, and $M_s = 5.8\times10^5$ A/m is the saturation magnetization. $\langle\boldsymbol{ij}\rangle$ denotes the nearest-neighbor sites. The first term is the AFM exchange interaction with the exchange stiffness $J_{ij} > 0$. An interfacial DMI $\boldsymbol{D}_{ij} = D_{ij}\hat{r}_{ij}\times\hat{z}$ stabilizes AFM skyrmions, where D_{ij} is the DMI constant and $\hat{r}_{ij}$ is the unit vector from site $\boldsymbol{i}$ to $\boldsymbol{j}$. The third term is the easy-axis anisotropic energy with $K_{\boldsymbol{I}} > 0$, while the final term represents the dipole-dipole interaction (DDI). In principle, disorders can be introduced through the AFM exchange interactions, the DMIs, and the anisotropic energies. We first consider random anisotropic energies and will discuss more general situations with random anisotropic energies, exchange interactions, and DMIs later. The disordered anisotropic energy $K_{\boldsymbol{I}}$ in the $\boldsymbol{I}$th grain distributes randomly and uniformly in the range of $[K_0 - \lambda K_0, K_0 + \lambda K_0]$ with $K_0 = 5$ meV. λ measures the disorder strength of the anisotropic energies. Exchange stiffness $J_{ij} = 94$ meV and DMI coefficient $D_{ij} = 25$ meV are constants. The model parameters used here can host AFM skyrmions and mimic synthetic antiferromagnets of (Pt/Co/Ru)-based multilayers [21].

For a relatively weak disorder, say $\lambda < 0.3$, stable isolated skyrmions of average radius $R_s \approx 10$ nm can be created from a small nucleation domain. The average size of the grains is set to be comparable with the skyrmion radius, i.e., $\mathfrak{g} = R_s = 10$ nm, which should be the most interesting case because of the following reasons: If the grain size is much larger than the skyrmion radius, the AFM skyrmion is essentially in a homogeneous film with boundaries. In the opposite limit in which the grain size is much smaller than the skyrmion radius, the disorder effect will be averaged out and become less pronounced.

III. NUMERICAL RESULTS

The current-driven spin dynamics is govern by the Landau-Lifshitz-Gilbert (LLG) equation [50],

$$\dot{\boldsymbol{m}}_i = \frac{\gamma}{M_s a^3}\boldsymbol{m}_i\times\frac{\partial\mathcal{H}_{\rm AFM}}{\partial\boldsymbol{m}_i} + \alpha\boldsymbol{m}_i\times\dot{\boldsymbol{m}}_i + \boldsymbol{\tau}_{\rm CIP}. \quad (2)$$

Here, γ is the gyromagnetic ratio, and $\alpha = 0.1$ is the Gilbert damping coefficient. $\boldsymbol{\tau}_{\rm CIP} = -(\boldsymbol{u}\cdot\nabla)\boldsymbol{m}_i + \beta\boldsymbol{m}_i\times(\boldsymbol{u}\cdot\nabla)\boldsymbol{m}_i$ is the spin-transfer torque of Zhang-Li form [51], with the velocity of electron $\boldsymbol{u} = \mu_B\boldsymbol{j}_e/[eM_s(1+\beta^2)]$. μ_B, e, and $\beta = 0.3$ are the Bohr magneton, the electron charge, and the nonadiabatic coefficient, respectively. The motion of the AFM skyrmion under $\boldsymbol{\tau}_{\rm CIP}$ is solved by the MUMAX3 package [52].

An AFM skyrmion initially centered at (0,0) starts to move when a current $\boldsymbol{j}_e = (j_x, 0)$ is applied along the x direction. In the absence of disorder, the trajectory of the skyrmion center is exactly along the electron flow, as shown by the straight line in Fig. 1(c). The skyrmion center is defined as $\boldsymbol{R} = (R_x, R_y) = \iint q_1\boldsymbol{x}dxdy/\iint q_1 dxdy$, where $q_{1(2)} = \boldsymbol{m}_{1(2)}\cdot(\partial_x\boldsymbol{m}_{1(2)}\times\partial_y\boldsymbol{m}_{1(2)})$ is the topological charge density on sublattice 1 or 2, and $\boldsymbol{m}_1(\boldsymbol{x}, t)$ and $\boldsymbol{m}_2(\boldsymbol{x}, t)$ are, respectively, magnetization unit vectors of the two sublattices. The total Magnus force on the AFM skyrmion is zero because it is proportional to the total topological charge of $Q = \iint(q_1 + q_2)dxdy/(4\pi) = 0$ [26]. In the presence of finite disorders, the AFM skyrmion deviates from $y = 0$; see one representative example shown in Fig. 1(d). The transverse motion of the AFM skyrmion is diffusive since its mean squared displacement increases with time t. Further micromagnetic simulations, discussed later, demonstrate that this diffusive behavior is very general and true when disorders are from other model parameters.

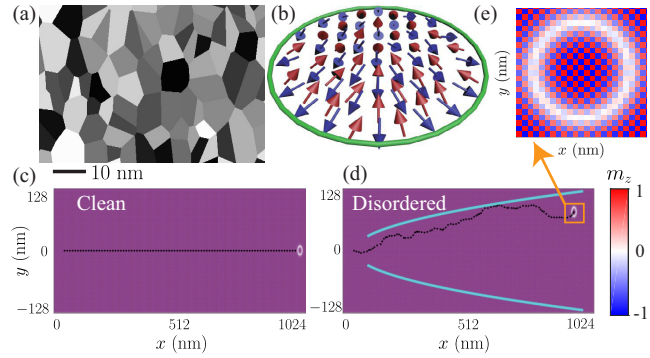

FIG. 1. (a),(b) Schematic illustration of (a) a granular film of an average grain size $\mathfrak{g} = 10$ nm and (b) an AFM skyrmion. (c), (d) AFM skyrmion trajectories driven by a current density of $j_x = 0.5\times10^{12}$ A/m^2 for (c) a clean film of $\lambda = 0$ and (d) a disordered film of $\lambda = 0.025$. The dashed lines denote the trajectories. The solid lines in (d) are the envelope of the AFM skyrmion trajectory. (e) Enlargement of the AFM skyrmion. Colors encode m_z.

Figure 2(a) is the time dependence of the ensemble average $\langle R_x\rangle$ (over more than 100 samples) for different λ. One can clearly see that $\langle R_x\rangle$ increases linearly with t and its slope decreases with λ for weak disorders of $\lambda = 0.03, 0.09, 0.12$. These results show that disorders always hinder the longitudinal motion, i.e., the hindering phase. As the disorder increases above a critical value of $\lambda_c \approx 0.15$, $\langle R_x\rangle$

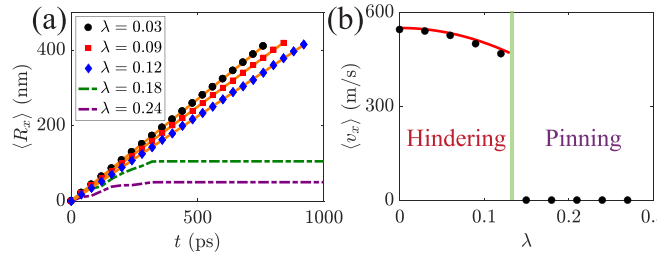

FIG. 2. (a) $\langle R_x\rangle$ as a function of t for $\lambda = 0.03, 0.09, 0.12, 0.18$, and 0.24. The orange lines are the linear fits of $\langle R_x\rangle = \langle v_x\rangle t$ for $\lambda = 0.03, 0.09$, and 0.12. (b) $\langle v_x\rangle$ vs λ for the two different phases. The solid line of the hindering phase is plotted by Eq. (5) without any fitting parameter. Here, $j_x = 2\times10^{12}$ A/m^2.

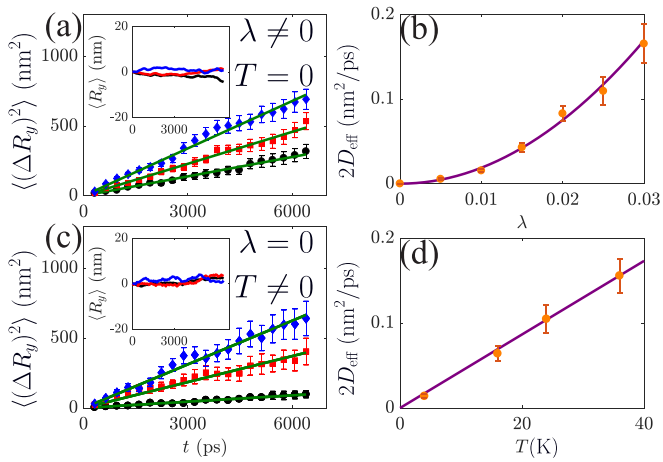

FIG. 3. (a) $\langle(\Delta R_y)^2\rangle$ and $\langle R_y\rangle$ (inset) as a function of t for $\lambda = 0.015, 0.02, 0.025$ (from bottom to top) and $T = 0$. The green solid lines are $\langle(\Delta R_y)^2\rangle = 2D_{\rm eff}t$ with fitted diffusion coefficients. (b) $2D_{\rm eff}$ as a function λ for $T = 0$. The solid line is Eq. (8). (c) Same as (a), but for $T = 4, 16, 24$ K (from bottom to top) and $\lambda = 0$. (d) $2D_{\rm eff}$ as a function of T for $\lambda = 0$. $\tilde{\alpha}$ is obtained by the χ^2 fit of $\log_{10}\langle(\Delta R_y)^2\rangle = \tilde{\alpha}\log_{10}t + \log_{10}(2D_{\rm eff})$, while $D_{\rm eff}$ is obtained by the linear fit of $\langle(\Delta R_y)^2\rangle = 2D_{\rm eff}t$, where we set $\tilde{\alpha} = 1$. Here, $j_x = 0.5\times10^{12}$ A/m^2.

approaches a constant, indicating a pinning phase for the AFM skyrmions. These are the cases of $\lambda = 0.18, 0.24 > \lambda_c$. A detailed analysis of the ensemble-average longitudinal velocity $\langle v_x\rangle$ obtained from the linear fit of the data above $t_0 \sim 400$ ps in Fig. 2(a) is presented in Fig. 2(b).

Figure 3(a) is a typical time evolution of mean transverse position $\langle R_y\rangle$ and mean square displacement $\langle(\Delta R_y)^2\rangle$ for different disorders $\lambda < \lambda_c$. Through a χ^2 fit of the numerical data in $t \in [80$ ps, 6640 ps$]$ to $\langle(\Delta R_y)^2\rangle = 2D_{\rm eff}t^{\tilde{\alpha}}$ with an acceptable goodness of fit $Q > 2\times10^{-3}$, we obtained $\tilde{\alpha} = 1.02 \pm 0.02, 1.09 \pm 0.02, 1.04 \pm 0.01$ for $\lambda = 0.015$ (black symbols), 0.02 (red symbols), and 0.025 (blue symbols), respectively. The green lines are linear fits to $\langle(\Delta R_y)^2\rangle = 2D_{\rm eff}t$. The excellent agreement between the data and the linear fits demonstrates that the transverse motion is a random walk with a zero mean, $\langle R_y\rangle = 0$, and the diffusion coefficient $D_{\rm eff}$. According to the orthodox theory, a stochastic motion with $\tilde{\alpha} = 1$ is a random walk, a superdiffusive (subdiffusive) motion with $\tilde{\alpha} > 1$ (<1) [53]. The dependence of $2D_{\rm eff}$ on λ is plotted in Fig. 3(b). A quadratic dependence, $2D_{\rm eff} \sim \lambda^2$, can be clearly seen.

The observed diffusion in transverse direction is strongly reminiscent of skyrmion diffusion under the thermal agitation [54,55]. This can be seen from the MUMAX3 simulations of an AFM skyrmion in a homogeneous film and in the presence of the finite temperature by setting $\lambda = 0$ and adding an additional torque in the LLG equation that characterizes the effect of thermal fluctuations, $\boldsymbol{\tau}_{\rm therm} = -[\gamma/(M_s a^3)]\boldsymbol{m}_i \times \boldsymbol{L}_i$ with the random field $\boldsymbol{L}_i$ of site i satisfying $\langle \boldsymbol{L}_i\rangle = \boldsymbol{0}$, and the fluctuation-dissipation theorem $\langle L_i^\mu(t)L_{i'}^\nu(t')\rangle = (2\alpha k_{\rm B}Ta^3M_s/\gamma)\delta_{\mu,\nu}\delta_{i,i'}\delta(t-t')$, with $k_{\rm B}$ being the Boltzmann constant [56]. Figure 3(c) shows the transverse mean squared displacement $\langle(\Delta R_y)^2\rangle$ of the AFM skyrmion at $T = 4, 16, 24$ K. It is hard to see differences between Fig. 3(a) and Fig. 3(c). Figure 3(d) shows that the thermal diffusion constant of an AFM skyrmion is proportional to T. Interestingly, the fitted $\tilde{\alpha}$ for the thermal diffusion takes values of $\tilde{\alpha} \in [0.95, 1.03]$. The green lines in Fig. 3(c) are the linear fits ($\tilde{\alpha} = 1$). This substantiates our assertion that the transverse motions of current-driven AFM skyrmions in a disordered film behave like a thermal diffusion with an effective temperature $T_{\rm eff}$. In the next section, we would like to determine this effective temperature $T_{\rm eff}$ based on the Thiele's rigid-body assumption.

IV. THEORETICAL ANALYSIS

To understand AFM skyrmion motion, we develop an effective theory in the continuous limit of our model (1). It is convenient to use the total magnetization $\boldsymbol{M} = \boldsymbol{M}_1 + \boldsymbol{M}_2$ and the Néel order $\boldsymbol{l} = \boldsymbol{M}_1 - \boldsymbol{M}_2$, with $\boldsymbol{n} = \boldsymbol{l}/|\boldsymbol{l}|$ unit vector of $\boldsymbol{l}$. There is one constraint of $\boldsymbol{n}\cdot\boldsymbol{M} = 0$ when $|\boldsymbol{M}_1| = |\boldsymbol{M}_2|$. The total energy of the thin film is given by $E_{\rm total} = a\iint \epsilon_{\rm total}dxdy$, with $\epsilon_{\rm total} = (A_M|\boldsymbol{M}|^2)/2 + A_N(\nabla\boldsymbol{n})^2 + (D/a^2)[n_z(\nabla\cdot\boldsymbol{n}) - (\boldsymbol{n}\cdot\nabla)n_z] + (K/a^3)(1-n_z^2)$ [57]. The first two terms are exchange energies of the magnetization and the Néel order with exchange constants A_M and A_N, respectively. The third term is the DMI for the Néel order, and the final term is the anisotropy with the random anisotropic constant $K = K(\boldsymbol{x})$. For the current-in-plane case, the dynamics of the Néel order is governed by [58]

$$\partial_{tt}\boldsymbol{n} = \tilde{\gamma}A_M[\gamma\boldsymbol{h}_{\boldsymbol{n}} - \alpha l\partial_t\boldsymbol{n} - \beta l(\boldsymbol{u}\cdot\nabla)\boldsymbol{n}], \tag{3}$$

with the effective field $\boldsymbol{h}_{\boldsymbol{n}} = -\delta E_{\rm total}/\delta\boldsymbol{n}$, $\tilde{\gamma} = \gamma/(1+\alpha^2)$, and $l = |\boldsymbol{l}| \sim M_s$. Hereafter, we take $\tilde{\gamma} \approx \gamma$ since $\alpha \ll 1$. The demagnetizing field of an ultrathin magnetic film just modifies the anisotropy [59]. We have carried out numerical simulations both with and without the DDI, and no significant difference is observed; see one representative example in Appendix A. Thus, the DDI is ignored below.

Recent studies show that the slow motion of an isolated AFM skyrmion can be well described by the Thiele's approach of the rigid-body approximation, i.e., $\boldsymbol{n}(\boldsymbol{x},t) = \boldsymbol{n}[\boldsymbol{x} - \boldsymbol{R}(t)]$ [26,38]. Under the rigid-body assumption and after some algebra, we obtain the following stochastic Thiele equation of the AFM skyrmion (see Appendix B):

$$\overleftrightarrow{\mathfrak{M}}\cdot\boldsymbol{a} + \alpha\overleftrightarrow{\mathfrak{D}}\cdot\boldsymbol{v} = \beta\overleftrightarrow{\mathfrak{D}}\cdot\boldsymbol{u} + \boldsymbol{f}. \tag{4}$$

Here, $\overleftrightarrow{\mathfrak{M}} = \overleftrightarrow{\mathfrak{D}}/(l\gamma A_M)$ is the effective mass tensor. $\overleftrightarrow{\mathfrak{D}}_{ij} = \iint \partial_i\boldsymbol{n}\cdot\partial_j\boldsymbol{n}dxdy$ is the dissipative dyadic. For a circularly symmetric AFM skyrmion, $\overleftrightarrow{\mathfrak{D}}_{ij} = \mathfrak{D}\delta_{ij}$ approximately. $\boldsymbol{v} = \dot{\boldsymbol{R}}$ and $\boldsymbol{a} = \ddot{\boldsymbol{R}}$ are the velocity and the acceleration of the AFM skyrmion, respectively. $\boldsymbol{f} = -\gamma\nabla_{\boldsymbol{R}}E_{\rm total}/(la) \approx N\gamma\nabla K/(la^3)$ with $N = \iint(1-n_z^2)dxdy$ is a stochastic force coming from the random anisotropy. We estimate $\mathfrak{D}$ and N by assuming a linear profile of the Néel vector and a constant shape of the AFM skyrmion [34,60]. In the clean system of $\lambda = 0$, $\boldsymbol{f} = 0$ and $\boldsymbol{v} = \boldsymbol{v}_0 = \beta(1-e^{-t/\tau})\boldsymbol{u}/\alpha$ with the characteristic time $\tau = 1/(\gamma l\alpha A_M)$. The time of our simulations is much longer than τ such that the skyrmion is in its steady state of $\boldsymbol{v}_0 = \beta\boldsymbol{u}/\alpha$.

A. Motion in the hindering phase

We now study the AFM skyrmion motion in the hindering phase where $\boldsymbol{u} = (u_x, 0)$ and $|\beta u_x/\alpha| \gg |f_x|/(\alpha\mathfrak{D})$ and focus first on the longitudinal motion. The longitudinal velocity at $t \gg \tau$ can be calculated by Eq. (4) (the inertial term is irrelevant for the steady state). The result is $v_x(t) = \beta u_x/\alpha + f_x(t)/(\alpha\mathfrak{D})$, indicating that the AFM skyrmion is boosted (hindered) by disorders when $f_x(t) > 0$ ($f_x(t) < 0$). If $\overline{\cdots}$ denotes the time average, then the time-average velocity is $\overline{v_x} = \beta u_x/\alpha + \overline{f_x}/(\alpha\mathfrak{D})$. For a long-distance $\mathcal{L}$ motion, it is reasonable to assume that the regimes of $f_x > 0$ and $f_x < 0$ appear with an equal possibility such that $\overline{f_x} = [1/(t_+ + t_-)]\int[f_x(1/v_{x+} + 1/v_{x-})]dx$ [47]. Here, $v_{x\pm}$ and $t_\pm = \mathcal{L}/(2v_{x\pm})$ are the velocities and the total traveling times of the AFM skyrmion in the boosting and the hindering regimes, respectively. After some calculations, with details given in Appendix B, we obtain $\overline{f_x} = -2\gamma^2N^2\lambda^2K_0^2/(3\beta u_x\mathfrak{D}l^2\mathfrak{g}^2a^6)$ up to the order of λ^2. As expected, $\overline{f_x}$ behaves as a friction that always hinders skyrmion motion: Although the distances for boosting and hindering are equal, the time of hindering, t_-, is always larger than that of boosting t_+ since $v_{x+} > v_{x-}$. Hence, AFM skyrmions are slowed down by disorders for long enough time. This feature can be clearly seen from the time-average longitudinal velocity $\overline{v_x}$ obtained by Eq. (4),

$$\overline{v_x} = \frac{\beta u_x}{\alpha} - \frac{2\gamma^2N^2\lambda^2K_0^2}{3\alpha\beta u_x\mathfrak{D}^2l^2\mathfrak{g}^2a^6}. \tag{5}$$

Indeed, Eq. (5) accords perfectly with the ensemble-average velocity $\langle v_x\rangle$ from simulations [red solid line in Fig. 2(b); no fitting was performed]. Noticeably, $\overline{v_x}$ approaches $v_{0x} = \beta u_x/\alpha$ in the limit of $u_x \to \infty$, indicating that the disorder effect is negligible for high driven current. This conclusion is further confirmed by numerical calculations; see Appendix C.

Next, we elucidate the diffusive motion in the transverse direction and derive the effective temperature $T_{\rm eff}$. For weak disorders, the AFM skyrmion moves linearly with time along the x direction. The stochastic transverse force f_y is the y component of the gradient of skyrmion energy, or the gradient of $K(\boldsymbol{x})$ at the skyrmion center. For the granular system, let us consider two pairs of nearest-neighbor grains at (x_1, y_1), (x_1, y_2), (x_2, y_1), and (x_2, y_2) along the y direction. The magnetic anisotropy energies satisfy $\langle K(x, y)\rangle = K_0$ and $\langle[K(x_1, y_1) - K(x_1, y_2)][K(x_2, y_1) - K(x_2, y_2)]\rangle = 2\mathfrak{g}(\lambda K_0)^2\delta(x_1 - x_2)/3$. For small disorders, we assume that $x_1 - x_2 \approx \beta u_x(t_1 - t_2)/\alpha$ such that $\overline{f_y(t)} = 0$ and

$$\overline{f_y(t_1)f_y(t_2)} = \frac{2\zeta_{\rm eff}k_{\rm B}T_{\rm eff}\gamma}{la}\delta(t_1 - t_2), \tag{6}$$

with the effective temperature being

$$T_{\rm eff} = \frac{\alpha\gamma N^2\lambda^2K_0^2}{3\zeta_{\rm eff}k_{\rm B}\mathfrak{g}l\beta u_x a^5} \tag{7}$$

and the friction coefficient $\zeta_{\rm eff} = \alpha\mathfrak{D}$ (see Appendix B). Then, the y component of Eq. (4) becomes the standard one-dimensional Langevin equation, i.e., $\mathfrak{D}a_y/(l\tilde{\gamma}A_M) = -\alpha\mathfrak{D}v_y + f_y(t)$. It is seen that rather than moving straightly along the x direction, the AFM skyrmion experiences a free Brownian motion caused by random anisotropies in the transverse direction. By solving the Langevin equation [61], we obtain $\langle(\Delta R_y)^2\rangle = 2D_{\rm eff}[t - \tau(1 - e^{-t/\tau})]$ with the diffusion coefficient reading

$$D_{\rm eff} = \frac{\gamma k_{\rm B}T_{\rm eff}}{la\zeta_{\rm eff}}. \tag{8}$$

As mentioned before, the time of our simulation (∼1 ns) is, in general, much larger than the relaxation time $\tau \approx 2.2$ ps such that $\langle(\Delta R_y)^2\rangle \simeq 2D_{\rm eff}t$, which explains the diffusive motions shown in Fig. 3(a). We compare Eq. (8) with the numerically obtained diffusion coefficients in Fig. 3(b) (purple line) and find a satisfactory agreement. Furthermore, we find no skyrmion size dependence of the effective temperature $T_{\rm eff}$. The transverse diffusion of an AFM skyrmion due to the disorders in the hindering phase is equivalent to the skyrmion motion under the thermal agitation described by the stochastic LLG equation at finite T. The meaning of our effective temperature $T_{\rm eff}$ is about this equivalence. However, the equivalence between the spatial randomness of model parameters and temporal randomness from an effective temperature makes sense only when a skyrmion can experience the spatial inhomogeneity. In other words, the equivalence fails in the pinning phase where a skyrmion has no way to know the spatial inhomogeneity.

In the examples considered so far, an AFM skyrmion moves in either a random anisotropic field or a fluctuating thermal field. In reality, both types of fields appear simultaneously. In the presence of both finite temperature and disorders, our theory can be generalized and AFM skyrmions still undergo a random walk in the transverse direction, i.e., $\langle(\Delta R_y)^2\rangle = 2D_{\rm eff}t$, with the diffusion coefficient given by $D_{\rm eff} = (\gamma k_{\rm B}\tilde{T})/(la\zeta_{\rm eff})$, similar to Eq. (8), but with the temperature modified as $\tilde{T} = T + T_{\rm eff} = T + (\alpha\gamma N^2\lambda^2K_0^2)/(3\zeta_{\rm eff}k_{\rm B}\mathfrak{g}l\beta u_x a^5)$ with T being the real temperature and $T_{\rm eff}$ being the effective temperature contributed by disorders. We have justified our theory by performing simulations with $\lambda \neq 0$ and $T \neq 0$ and the results are summarized in Appendix D.

B. Critical disorder

Numerical simulations in Fig. 2(a) show the pinning of AFM skyrmions by strong disorders. The critical disorder λ_c separating the hindering phase from the pinning phase is given by $|\beta u_x/\alpha| = \max[|f_x|/(\alpha\mathfrak{D})]$. The force on an AFM skyrmion due to the random magnetic anisotropy is $|K_I - K_J|/\mathfrak{g}$. The maximal random force should be larger than the driven term $\beta\mathfrak{D}u_x$ in order to pin the AFM skyrmions such that $\overline{v_x}$ in Eq. (4) becomes zero,

$$\beta\mathfrak{D}u_x = \frac{\gamma N|K_I - K_J|}{l\mathfrak{g}a^3} \approx \frac{2\lambda_c K_0\gamma N}{l\mathfrak{g}a^3}. \tag{9}$$

For a given driven current j_x, the critical disorder strength thus reads $\lambda_c = \beta\mathfrak{D}l\mathfrak{g}\mu_B j_x a^3/[2\gamma NK_0eM_s(1 + \beta^2)]$, which also accords well with numerical simulations as shown in Fig. 4 that depict λ_c as a function of j_x for the same other parameters used in Fig. 2.

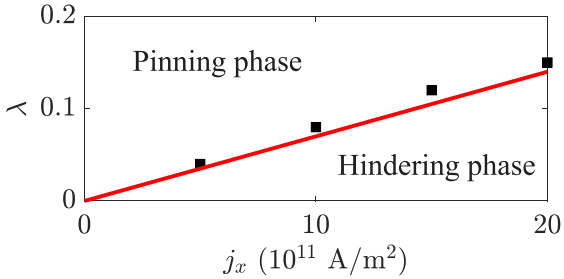

FIG. 4. Phase diagram in the $j_x - \lambda$ plane. The phase boundary (solid line) is plotted according to Eq. (8). The black squares are determined through simulations.

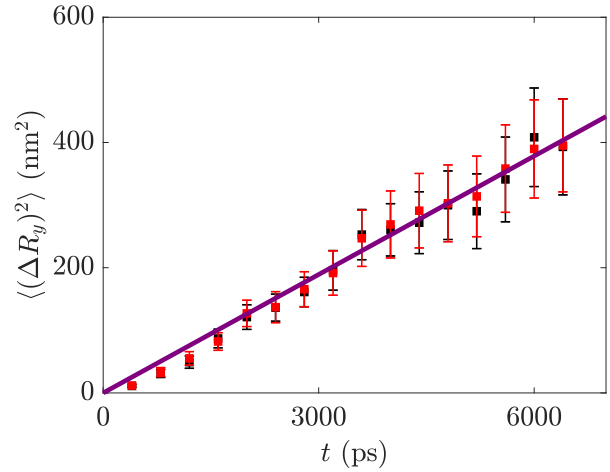

FIG. 5. $\langle(\Delta R_y)^2\rangle$ as a function of t for $\lambda = 0.15$ and $T = 0$. The black and red squares are data with and without the DDIs, respectively. The purple solid line is $\langle(\Delta R_y)^2\rangle = 2D_{\rm eff}t$, with the diffusion coefficient determined by Eq. (7). Each point is the average over more than 100 samples. Here, $j_x = 0.5\times10^{12}$ A/m^2.

V. DISCUSSION AND CONCLUSION

Before concluding, we would like to make a remark about disorders. Although the diffusive transverse motion of an AFM skyrmion in the hindering phase is obtained with random magnetic anisotropy, the similar diffusive motion is generally true for other random model parameters. In Appendix E, we generalize our theory by modeling the granular film with random distributed exchange stiffness and DMI constant in the range of $[J_0 - \nu J_0, J_0 + \nu J_0]$ and $[D_0 - \xi D_0, D_0 + \xi D_0]$ of each grain, respectively. After some algebra (see Appendix E), we find that the effective temperature of the AFM skyrmion in the hindering phase is

$$T_{\rm eff} = \frac{\alpha\gamma a}{3\zeta_{\rm eff}k_{\rm B}\mathfrak{g}l\beta u_x}\left(\frac{C_1^2\nu^2J_0^2}{a^2} + \frac{N^2\lambda^2K_0^2}{a^6} + \frac{C_2^2\xi^2D_0^2}{a^4}\right), \quad (10)$$

with $C_1 = \iint(\nabla\boldsymbol{n})^2dxdy = \mathfrak{D}_{xx} + \mathfrak{D}_{yy}$ and $C_2 = \iint[n_z(\nabla\cdot\boldsymbol{n}) - (\nabla\cdot\boldsymbol{n})n_z]dxdy$ depending on the profile of the AFM skyrmion. It is seen that the contributions from random exchange interactions, anisotropy energies, and DMIs to the effective temperature are the first, second, and third terms of Eq. (10), respectively. Therefore, such diffusive transverse motion should also be applicable for not only Hamiltonian (1), but also a general granular film with different parameters (exchange stiffness, DMI constants, and anisotropic energies) in different grains. One can find numerical supports to this argument in Appendix E.

In summary, we have revealed the disorder effects on the current-driven AFM skyrmion dynamics. Weak disorders always hinder the longitudinal motion and make an AFM skyrmion undergo a random walk along the transverse direction. The results can be well explained by the stochastic Thiele equation. Strong disorders above a critical strength pin AFM skyrmions. Our findings are important for future AFM skyrmion devices.

ACKNOWLEDGMENTS

K.Y.J. and C.W. contributed equally to this work. This work is supported by the National Natural Science Foundation of China (Grants No. 11774296, No. 11704061, and No. 11974296) and Hong Kong RGC (Grants No. 16301518 and No. 16301619).

APPENDIX A: EFFECT OF DDIs

We have carried out simulations with and without the DDI and found no obvious difference between the two cases, just like the general belief that the stray field in an AFM thin film is negligible [38]. One representative example is shown in Fig. 5 that displays $\langle(\Delta R_y)^2\rangle$ as a function of time for $\lambda = 0.15$ and $T = 0$ with (black squares) and without (red squares) the DDIs. It is seen that the two curves merge, indicating that the DDI plays an insignificant role in the diffusive behavior of the AFM skyrmion. In addition, the two curves accord well with the analytical result (purple line).

We give a coherent explanation for the numerical results shown in Fig. 5. The DDIs cause a demagnetization field $\boldsymbol{H}_{\rm demag}$ with the contributions from both bulk charges and surface charges. For the thin film of size $L_xa\times L_ya\times a$ studied in this work ($L_x, L_y \gg 1$), it is shown that the contribution of the bulk charge is negligible compared with that of the surface charge based on the assumption that the magnetization is uniform in the z direction [59]. Hence, the demagnetization field can be written as

$$\boldsymbol{H}^{\rm A(B)}_{\rm demag}(\boldsymbol{r}) \approx \frac{M_s}{4\pi}\left\{\int[\hat{z}\cdot\boldsymbol{m}_{\rm A(B)}(\boldsymbol{r}')]\frac{\boldsymbol{r}-\boldsymbol{r}'}{|\boldsymbol{r}-\boldsymbol{r}'|^3}dS'_+ + \int[\hat{z}\cdot\boldsymbol{m}_{\rm A(B)}(\boldsymbol{r}')]\frac{\boldsymbol{r}-\boldsymbol{r}'}{|\boldsymbol{r}-\boldsymbol{r}'|^3}dS'_-\right\}, \quad (A1)$$

with $\boldsymbol{H}^{\rm A(B)}_{\rm demag}(\boldsymbol{r})$ being the demagnetization field of the $A(B)$ sublattices of a point $\boldsymbol{r} = (\boldsymbol{r}_\parallel, 0)$ in the thin film. S'_+ and S'_- are the top and bottom surfaces of the thin film (the planes of $z = a/2$ and $z = -a/2$), respectively. $\boldsymbol{r}' = (\boldsymbol{r}'_\parallel, 0)$ is the variable to be integrated over the surfaces. For the in-plane components

of the demagnetization field, we have

$$\boldsymbol{H}^{\mathrm{A(B)}}_{\mathrm{demag},\parallel} = \frac{M_s}{4\pi}\Bigg[\int \frac{(\hat{z}\cdot\boldsymbol{m}_{\mathrm{A(B)}})(\boldsymbol{r}_\parallel - \boldsymbol{r}'_\parallel)}{(|\boldsymbol{r}_\parallel - \boldsymbol{r}'_\parallel|^2 + a^2/4)^{3/2}} d\boldsymbol{r}'_\parallel - \int \frac{(\hat{z}\cdot\boldsymbol{m}_{\mathrm{A(B)}})(\boldsymbol{r}_\parallel - \boldsymbol{r}'_\parallel)}{(|\boldsymbol{r}_\parallel - \boldsymbol{r}'_\parallel|^2 + a^2/4)^{3/2}} d\boldsymbol{r}'_\parallel\Bigg] = 0; \quad \text{(A2)}$$

while for the z component,

$$\begin{aligned} H^{\mathrm{A(B)}}_{\mathrm{demag},z} &= \frac{M_s}{4\pi}\Bigg[\int \hat{z}\cdot\boldsymbol{m}_{\mathrm{A(B)}}(r')\frac{-(a/2)}{(|\boldsymbol{r}_\parallel - \boldsymbol{r}'_\parallel|^2 + a^2/4)^{3/2}} d\boldsymbol{r}'_\parallel \\ &\quad - \int \hat{z}\cdot\boldsymbol{m}_{\mathrm{A(B)}}(r')\frac{(a/2)}{(|\boldsymbol{r}_\parallel - \boldsymbol{r}'_\parallel|^2 + a^2/4)^{3/2}} d\boldsymbol{r}'_\parallel\Bigg] \\ &= -\frac{M_s}{4\pi}\int \hat{z}\cdot\boldsymbol{m}_{\mathrm{A(B)}}\frac{a}{(|\boldsymbol{r}_\parallel - \boldsymbol{r}'_\parallel|^2 + a^2/4)^{3/2}} d\boldsymbol{r}'_\parallel. \end{aligned} \quad \text{(A3)}$$

Equations (A2) and (A3) indicate that the demagnetization field of the AFM thin film acts like an external magnetic field in the z direction, i.e., $\boldsymbol{H}_{\mathrm{demag}} = (0, 0, H_{\mathrm{demag},z})$ with $H_{\mathrm{demag},z} = H^A_{\mathrm{demag},z} + H^B_{\mathrm{demag},z}$. It is reasonable to assume that the magnetizations are antiparallel in the thin film, i.e., $\boldsymbol{m}_{\mathrm{A}}(\boldsymbol{r}) = -\boldsymbol{m}_{\mathrm{B}}(\boldsymbol{r})$. Thus, $H_{\mathrm{demag},z} \approx 0$, i.e., $\boldsymbol{H}^{\mathrm{A}}_{\mathrm{demag}}$ and $\boldsymbol{H}^{\mathrm{B}}_{\mathrm{demag}}$ cancel with each other.

APPENDIX B: STOCHASTIC THIELE EQUATION

In this Appendix, we derive the stochastic Thiele equation for the AFM skyrmion in the granular film. Let us begin with the effective field of the Néel vector in the continuous limit,

$$\begin{aligned} \boldsymbol{h}_{\boldsymbol{n}} &= -\frac{\delta E_{\mathrm{total}}}{\delta \boldsymbol{n}} \\ &= 2A_N\nabla^2\boldsymbol{n} + (2K/a^3)n_z\hat{z} \\ &\quad + (2D/a^2)(\partial_x n_z, \partial_y n_z, -\partial_x n_x - \partial_y n_y). \end{aligned} \quad \text{(B1)}$$

We adapt the rigid-body assumption that $\boldsymbol{n}(\boldsymbol{x}, t) = \boldsymbol{n}[\boldsymbol{x} - \boldsymbol{R}(t)]$, with $\boldsymbol{R}(t)$ being the position of the center of the AFM skyrmion [49]. Under this assumption,

$$\partial_t\boldsymbol{n} = -(\boldsymbol{v}\cdot\nabla)\boldsymbol{n}, \partial_{tt}\boldsymbol{n} = -(\boldsymbol{a}\cdot\nabla)\boldsymbol{n}, \quad \text{(B2)}$$

with $\boldsymbol{v} = \dot{\boldsymbol{R}}$ and $\boldsymbol{a} = \ddot{\boldsymbol{R}}$ being the velocity and the acceleration of the AFM skyrmion, respectively. Then, we write the dynamics of the Néel vector [given by Eq. (3)] as

$$\begin{aligned} 0 &= \frac{1}{\gamma^2 l}(\boldsymbol{a}\cdot\nabla)\boldsymbol{n} + \frac{A_M}{l}\boldsymbol{h}_{\boldsymbol{n}} \\ &\quad + \frac{A_M}{\gamma}(\boldsymbol{v}'\cdot\nabla)\boldsymbol{n} \quad = \boldsymbol{H}_1 + \boldsymbol{H}_2 + \boldsymbol{H}_3, \end{aligned} \quad \text{(B3)}$$

with $\boldsymbol{v}' = \alpha\boldsymbol{v} - \beta\boldsymbol{u}$ being a renormalized velocity. Here, we use the fact that $\alpha \ll 1$ such that $\tilde{\gamma} = \gamma/(1+\alpha^2) \approx \gamma$. From Eq. (B3), we introduce the force density (in terms of components) as

$$f_{1,i} = -lH_{1,j}\frac{\partial n_j}{\partial x_i} = -\frac{1}{\gamma^2}a_k\frac{\partial n_j}{\partial x_k}\frac{\partial n_j}{\partial x_i}, \quad \text{(B4)}$$

$$f_{2,i} = -lH_{2,j}\frac{\partial n_j}{\partial x_i} = -A_M h_{\boldsymbol{n},j}\frac{\partial n_j}{\partial x_i}, \quad \text{(B5)}$$

and

$$f_{3,i} = -lH_{3,j}\frac{\partial n_j}{\partial x_i} = -\frac{lA_M}{\gamma}v'_k\frac{\partial n_j}{\partial x_k}\frac{\partial n_j}{\partial x_i}. \quad \text{(B6)}$$

Equation (B3) can therefore be written as $\sum_{i=1}^3 \boldsymbol{f}_i = 0$. Next, we integrate this equation over the entire AFM skyrmion,

$$0 = \iint (\boldsymbol{f}_1 + \boldsymbol{f}_2 + \boldsymbol{f}_3)dxdy. \quad \text{(B7)}$$

It is easy to find that the second term of Eq. (B7) reads

$$\iint \boldsymbol{f}_2 dxdy = -\frac{A_M}{a}\nabla_{\boldsymbol{R}}E_{\mathrm{total}}, \quad \text{(B8)}$$

with $E_{\mathrm{total}} = a\iint\{A_N(\nabla\boldsymbol{n})^2 + (K/a^3)(1-n_z^2) + (D/a^2)[n_z(\nabla\cdot\boldsymbol{n}) - (\boldsymbol{n}\cdot\nabla)n_z]\}dxdy$. To evaluate the first term and the third term in Eq. (B3), we introduce the dissipative density tensor $\overleftrightarrow{d}$ with $d_{ij} = \partial_{x_i}\boldsymbol{n}\cdot\partial_{x_j}\boldsymbol{n}$ such that

$$\boldsymbol{f}_1 = -\frac{1}{\gamma^2}\overleftrightarrow{d}\cdot\boldsymbol{a} \quad \text{(B9)}$$

and

$$\boldsymbol{f}_3 = -\frac{lA_M}{\gamma}\overleftrightarrow{d}\cdot\boldsymbol{v}'. \quad \text{(B10)}$$

We then recast Eq. (B7) as

$$-\frac{1}{l\gamma A_M}\overleftrightarrow{\mathfrak{D}}\cdot\boldsymbol{a} - \frac{\gamma}{la}\nabla_{\boldsymbol{R}}E_{\mathrm{total}} - \overleftrightarrow{\mathfrak{D}}\cdot\boldsymbol{v}' = 0, \quad \text{(B11)}$$

with $\overleftrightarrow{\mathfrak{D}} = \iint\overleftrightarrow{d}dxdy$ being the dissipative dyadic. By defining the effective mass tensor $\overleftrightarrow{\mathfrak{M}} = \overleftrightarrow{\mathfrak{D}}/(l\gamma A_M)$, we obtain the dynamics equation of the AFM skyrmion,

$$\overleftrightarrow{\mathfrak{M}}\cdot\boldsymbol{a} + \alpha\overleftrightarrow{\mathfrak{D}}\cdot\boldsymbol{v} = \beta\overleftrightarrow{\mathfrak{D}}\cdot\boldsymbol{u} + \boldsymbol{f}, \quad \text{(B12)}$$

with $\boldsymbol{f} = -\gamma\nabla_{\boldsymbol{R}}E_{\mathrm{total}}/(la)$. Equation (B12) is Eq. (4) in Sec. IV. Here, we just consider the cases of random anisotropic energies while the exchange interactions and the DMIs are constants such that

$$\boldsymbol{f} = -\frac{\gamma\nabla_{\boldsymbol{R}}E_{\mathrm{total}}}{la} \approx \frac{N\gamma\nabla K(\boldsymbol{x})}{la^3}, \quad \text{(B13)}$$

with $N = \iint(1-n_z^2)dxdy$. Here, we have assumed that the profile of the skyrmion stays unchanged, whose validity is confirmed by numerical calculations (not shown here).

First, let us evaluate the x component of $\boldsymbol{f}$. For the AFM skyrmion propagating a long distance $\mathcal{L}$ that is much larger than the average grain size $\mathfrak{g}$, it is reasonable to assume that the regimes of $f_x > 0$ (boosting) and $f_x < 0$ (hindering) appear with an equal probability. The velocity of the AFM skyrmion in the boosting and the hindering regimes can be solved by Eq. (B12) (here we ignore the mass term since we consider the long-time dynamics), say, $v_{x,\pm} = \beta u_x/\alpha \pm$

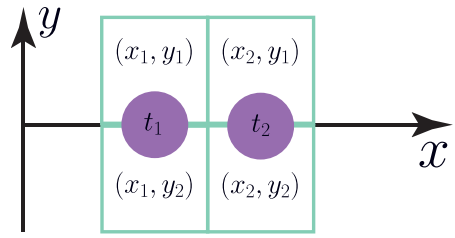

FIG. 6. Schematic plot of the origin of the transverse stochastic force $f_y(t)$. We assume that the AFM skyrmion (purple circle) moves in a straight line (here it is $y = 0$). At t_1 (t_2), the stochastic force acting on the AFM skyrmion in the transverse direction comes from the differences of the magnetic anisotropic energies of the grains (x_1, y_1) and (x_1, y_2) [(x_2, y_1) and (x_2, y_2)].

$|f_x|/(\alpha\mathfrak{D})$. The total times of the AFM skyrmion in the boosting and the hindering regimes are thus $t_\pm = \mathcal{L}/(2v_{x,\pm})$. Then,

$$\overline{f_x} = \frac{1}{t_+ + t_-}\left(\int_0^{\mathcal{L}/2}\frac{|f_x|}{v_{x,+}}dx + \int_0^{\mathcal{L}/2}\frac{-|f_x|}{v_{x,-}}dx\right) \approx -\frac{2}{\mathcal{L}\beta u_x\mathfrak{D}}\int_0^{\mathcal{L}/2}|f_x|^2dx \approx -\frac{\gamma^2N^2}{\beta u_x\mathfrak{D}l^2\mathfrak{g}^2a^6}\langle(K_I - K_J)^2\rangle. \tag{B14}$$

Note that K_I is a white noise and distributes randomly in the range $[K_0 - \lambda K_0, K_0 + \lambda K_0]$. Therefore, $\langle K_I\rangle = K_0$ and $\langle(K_I - K_0)(K_J - K_0)\rangle = (\lambda^2K_0^2/3)\delta_{IJ}$. We then have $\langle K_I - K_J\rangle = 0$ and

$$\langle(K_I - K_J)^2\rangle = \frac{2\lambda^2K_0^2}{3} \tag{B15}$$

[note that $I \neq J$ in Eq. (B15)]. Substituting Eq. (B15) to Eq. (B14), we finally obtain the time-average velocity,

$$\overline{v_x} = \frac{\beta}{\alpha}u_x - \frac{2\gamma^2N^2\lambda^2K_0^2}{3\alpha\beta u_x\mathfrak{D}^2l^2\mathfrak{g}^2a^6}. \tag{B16}$$

Equation (B16) is Eq. (5) in Sec. IV A.

Second, we consider the y component of the stochastic force which is contributed by the differences of magnetic anisotropy energies along the y direction. For two pairs of neighbor grains along the y direction at positions x_1 and x_2 (see Fig. 6), the magnetic anisotropic energy satisfies

$$\langle[K(x_1, y_1) - K(x_1, y_2)][K(x_2, y_1) - K(x_2, y_2)]\rangle = \frac{2\lambda^2K_0^2}{3}\mathfrak{g}\delta(x_1 - x_2) \tag{B17}$$

and $\langle[K(x_1, y_1) - K(x_1, y_2)]\rangle = \langle[K(x_2, y_1) - K(x_2, y_2)]\rangle = 0$. The stochastic force in the y direction at x_1 and x_2 thus reads

$$f_y(x_1) = -\frac{\gamma}{la}\frac{\partial E_{\text{total}}}{\partial R_y}\bigg|_{x=x_1} \approx -\frac{\gamma N}{la^3}\frac{K(x_1, y_2) - K(x_1, y_1)}{\mathfrak{g}},$$
$$f_y(x_2) = -\frac{\gamma}{la}\frac{\partial E_{\text{total}}}{\partial R_y}\bigg|_{x=x_2} \approx -\frac{\gamma N}{la^3}\frac{K(x_2, y_2) - K(x_2, y_1)}{\mathfrak{g}}. \tag{B18}$$

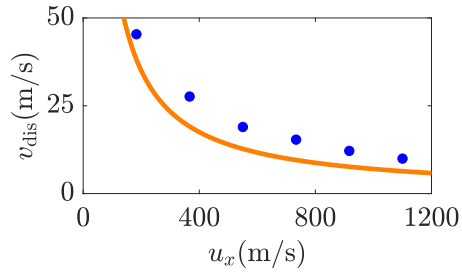

FIG. 7. v_{dis} as a function of λ obtained by simulations. The solid line is plotted by Eq. (C1).

Clearly, $\langle f_y(x_1)\rangle = \langle f_y(x_2)\rangle = 0$. We further assume that $x_1 - x_2 \approx \beta u_x(t_1 - t_2)/\alpha$. Then,

$$\overline{f_y(t_1)f_y(t_2)} = \frac{2\lambda^2K_0^2\alpha\gamma^2N^2}{3l^2\mathfrak{g}\beta u_xa^6}\delta(t_1 - t_2). \tag{B19}$$

We define an effective temperature T_{eff} as

$$T_{\text{eff}} = \frac{\alpha\gamma N^2\lambda^2K_0^2}{3\zeta_{\text{eff}}k_{\text{B}}\mathfrak{g}l\beta u_xa^5}, \tag{B20}$$

with the friction coefficient $\zeta_{\text{eff}} = \alpha\mathfrak{D}$ and recast Eq. (B19) as

$$\overline{f_y(t_1)f_y(t_2)} = \frac{2\zeta_{\text{eff}}k_{\text{B}}T_{\text{eff}}\gamma}{la}\delta(t_1 - t_2). \tag{B21}$$

Equations (B19) to (B21) are Eqs. (6) and (7) in Sec. IV B.

APPENDIX C: LARGE CURRENT CASES

From Eq. (5) in Sec. IV A, we can clearly see two contributions to the longitudinal velocity of the AFM skyrmion v_x: The first term is due to the driven current, and the second term is from the disorder that always hinders the AFM skyrmion motion:

$$v_{\text{dis}} = \frac{2\gamma^2N^2\lambda^2K_0^2}{3\alpha\beta u_x\mathfrak{D}^2l^2\mathfrak{g}^2a^6}. \tag{C1}$$

Our theory shows that v_{dis} decreases with the increasing of u_x, i.e., the effect of disorders is strongly suppressed by applying a large current. To confirm this feature, we numerically calculate v_{dis} as a function of u_x for $\lambda = 0.09$, $\alpha = 0.1$. Other material parameters are the same as those in Fig. 3. As depicted in Fig. 7, the obtained v_{dis} (from micromagnetic simulations) decreases with the increasing of u_x and accords well with the analytical result given by Eq. (C1).

APPENDIX D: DISORDERED SYSTEMS AT FINITE TEMPERATURE

In this Appendix, we generalize our theory by considering the effect of both disorders and thermal fluctuations. To this end, we add an additional torque in Eq. (3),

$$\partial_{tt}\boldsymbol{n} = \gamma A_M[\gamma(\boldsymbol{h}_n + l\boldsymbol{\Theta}) - \alpha l\partial_t\boldsymbol{n} - \beta l(\boldsymbol{u}\cdot\nabla)\boldsymbol{n}], \tag{D1}$$

with the stochastic field $\boldsymbol{\Theta}$ satisfying the fluctuation-dissipation theorem [56], i.e., $\overline{\boldsymbol{\Theta}} = \boldsymbol{0}$ and

$$\overline{\Theta_i(\boldsymbol{x}, t)\Theta_j(\boldsymbol{x}', t')} = \frac{2\alpha k_{\text{B}}T}{\gamma la}\delta_{ij}\delta(\boldsymbol{x} - \boldsymbol{x}')\delta(t - t'). \tag{D2}$$

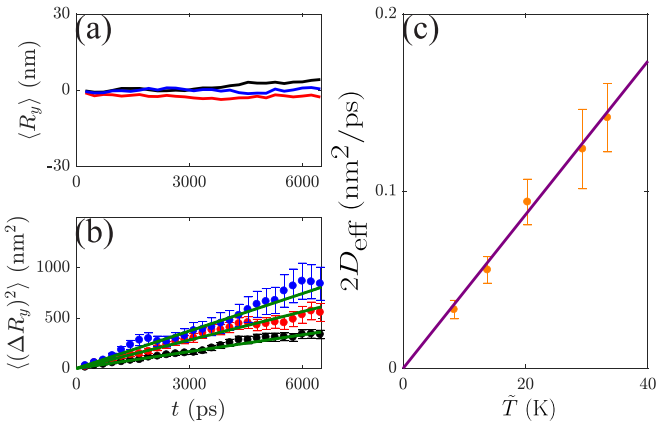

FIG. 8. (a) $\langle R_y \rangle$ and (b) $\langle (\Delta R_y)^2 \rangle$ as a function of t for different λ and T: $\lambda = 0.015$, $T = 4$ K (black), $\lambda = 0.01$, $T = 16$ K (red), and $\lambda = 0.01$, $T = 25$ K (blue). Green solid lines in (b) are the fits of $\langle (\Delta R_y)^2 \rangle = 2D_{\rm eff} t$. (c) Diffusion coefficient $2D_{\rm eff}$ as a function of $\tilde{T}$ obtained by simulations, with $\tilde{T}$ being calculated by Eq. (D8). Solid line is Eq. (D9). Here, $j_x = 0.5\times10^{12}$ A/m^2.

This torque can be recast as a thermal force in Eq. (B7) with the force density $-(A_M l \Theta_j \partial_{x_i} n_j)\hat{x}_i$. Thus, there is an additional force in Eq. (B12) contributed from the thermal fluctuations,

$$\overleftrightarrow{\mathfrak{M}} \cdot \boldsymbol{a} + \alpha \overleftrightarrow{\mathfrak{D}} \cdot \boldsymbol{v} = \beta \overleftrightarrow{\mathfrak{D}} \cdot \boldsymbol{u} + \boldsymbol{f} + \boldsymbol{f}_{\rm therm}. \tag{D3}$$

By integrating the force density and rearranging the coefficients, we obtain the pth component of the thermal force $\boldsymbol{f}_{\rm therm}$,

$$f_{p,\rm therm} = -\gamma \iint \Theta_j \frac{\partial n_j}{\partial x_p} dxdy, \tag{D4}$$

which satisfies the fluctuation-dissipation theorem,

$$\overline{f_{p,\rm therm}(t) f_{q,\rm therm}(t')} = \frac{2\alpha \mathfrak{D} \gamma k_{\rm B} T}{la} \delta(t-t') \delta_{p,q}. \tag{D5}$$

We are now interested in the transverse motion of the AFM skyrmion, i.e.,

$$\frac{\mathfrak{D}}{l\gamma A_M} \frac{dv_y}{dt} = -\alpha \mathfrak{D} v_y + f_y(t) + f_{y,\rm therm}(t). \tag{D6}$$

Let us introduce a new quantity $\tilde{f}_y(t) = f_y(t) + f_{y,\rm therm}(t)$. It is easy to find that

$$\overline{\tilde{f}_y(t) \tilde{f}_y(t')} = \frac{2\alpha \mathfrak{D} \gamma k_{\rm B} \tilde{T}}{la} \delta(t-t'), \tag{D7}$$

with a renormalized temperature being

$$\tilde{T} = T + T_{\rm eff} = T + \frac{\gamma N^2 \lambda^2 K_0^2}{3 l \mathfrak{g} \beta u_x \mathfrak{D} k_{\rm B} a^5}, \tag{D8}$$

where T is the real temperature and $T_{\rm eff}$ is the effective temperature contributed by disorders. Therefore, our analysis shows that in the presence of disorders at the finite temperature, the transverse motion of the AFM skyrmion is still a random walk with the diffusion coefficient $D_{\rm eff}$ being similar to Eq. (8) in Sec. IV A, but with a renormalized temperature of

$$D_{\rm eff} = \frac{\gamma k_{\rm B} \tilde{T}}{la\zeta_{\rm eff}}. \tag{D9}$$

To confirm our theory, we numerically calculate $\langle R_y \rangle$ and $\langle (\Delta R_y)^2 \rangle$ for various λ and T (real temperature) and plot some representative data in Figs. 8(a) and 8(b), respectively. By using the same numerical approach, we verify that $\langle (\Delta R_y)^2 \rangle = 2D_{\rm eff} t$, a typical feature of a one-dimensional random walk, and obtain the diffusion coefficients for different $\tilde{T}$ [calculated by Eq. (D8)] by performing a linear fit of the data. The obtained diffusion coefficients $2D_{\rm eff}$ for different $\tilde{T}$ are shown in Fig. 8(c), which accord well with our theory given by Eq. (D9).

APPENDIX E: RANDOM EXCHANGE INTERACTIONS AND DMIs

In Appendix B, we have analytically derived the effective temperature of the AFM skyrmion in the hindering phase by assuming the random anisotropic energies and the constant exchange interactions and the DMIs. In this Appendix, we generalize our theory by modeling the granular film with both random anisotropic energies and random exchange interactions and DMIs. In the continuous limit, we set the exchange constants A_N, the DMI constants D, and the anisotropic energies K distributed uniformly in the range of $[J_0 - \nu J_0, J_0 + \nu J_0]/a$, $[D_0 - \xi D_0, D_0 + \xi D_0]$, and $[K_0 - \lambda K_0, K_0 + \lambda K_0]$, respectively. Thus, the positive numbers ν, ξ, and λ measure the degrees of randomness of the exchange interactions, the DMIs, and the anisotropic energies, respectively. The stochastic force due to disorders thus reads

$$\boldsymbol{f} = -\frac{\gamma}{l} \nabla_{\boldsymbol{R}} \left(\iint \left\{ A_N (\nabla \boldsymbol{n})^2 + (K/a^3)\left(1 - n_z^2\right) + (D/a^2)[n_z(\nabla \cdot \boldsymbol{n}) - (\boldsymbol{n} \cdot \nabla) n_z] \right\} dxdy \right). \tag{E1}$$

Under the rigid-body assumption, Eq. (E1) can be recast as

$$\boldsymbol{f} = \frac{\gamma}{l} \left(C_1 \nabla A_N + \frac{N}{a^3} \nabla K + \frac{C_2}{a^2} \nabla D \right), \tag{E2}$$

with $C_1 = \iint (\nabla \boldsymbol{n})^2 dxdy = \mathfrak{D}_{xx} + \mathfrak{D}_{yy}$ and $C_2 = \iint [n_z(\nabla \cdot \boldsymbol{n}) - (\boldsymbol{n} \cdot \nabla) n_z] dxdy$ that are determined by the profile of the AFM skyrmion and stay nearly unchanged. Following the same approach as in Appendix B, we obtain

$$\overline{f_y(t_1) f_y(t_2)} = \frac{2\alpha\gamma^2}{3 l^2 \mathfrak{g} \beta u_x} \left(\frac{C_1^2 \nu^2 J_0^2}{a^2} + \frac{N^2 \lambda^2 K_0^2}{a^6} + \frac{C_2^2 \xi^2 D_0^2}{a^4} \right) \times \delta(t_1 - t_2). \tag{E3}$$

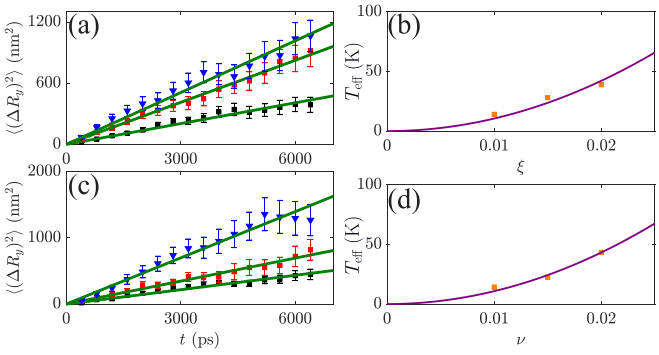

FIG. 9. (a) $\langle(\Delta R_y)^2\rangle$ as a function for t for $\xi = 0.01, 0.015, 0.02$ (from bottom to top) and $\nu = \lambda = 0$. Green lines are linear fits of the data. (b) $T_{\rm eff}$ as a function of ξ obtained by the data in (a). Purple line is a quadratic fit of the data, i.e., $T_{\rm eff} \propto \xi^2$. (c),(d) Same as (a),(b), but for $\nu = 0.01, 0.015, 0.02$ and $\xi = \lambda = 0$. Here, $j_x = 0.5\times10^{12}$ A/m^2.

From Eq. (E3), it is straightforward to find the effective temperature given by Eq. (10).

We also performed numerical simulations to support the above analyses. First, we set the strength of the DMI of each grain distributing randomly and uniformly in the range of $[D_0 - \xi D_0, D_0 + \xi D_0]$ with $D_0 = 25$ meV, while the anisotropic energy $K_0 = 5$ meV and the exchange stiffness $J_0 = 94$ meV of each grain are the same. The transverse motion of the skyrmion is illustrated in Fig. 9(a), which displays the transverse mean square displacement $\langle(\Delta R_y)^2\rangle$ as a function of time t. The transverse motion is also diffusive, i.e., $\langle(\Delta R_y)^2\rangle = 2D_{\rm eff}t$; see the linear fits of the numerical data (solid lines). Furthermore, we find a quadratic dependence between the effective temperature $T_{\rm eff}$ and the randomness ξ that agree qualitatively with Eq. (10); see Fig. 9(b). Very similar pictures have been found if we set the exchange stiffness J_{ij} distributing randomly in the range of $[J_0 - \nu J_0, J_0 + \nu J_0]$ while the DMI and the anisotropic energy are homogeneous, as shown in Figs. 9(c) and 9(d).

[1] A. N. Bogdanov and D. A. Yablonskii, Thermodynamically stable "vortices" in magnetically ordered crystals: The mixed state of magnets, Zh. Eksp. Teor. Fiz. **95**, 178 (1989) [Sov. Phys. JETP **68**, 101 (1989)].

[2] U. K. Rößler, A. N. Bogdanov, and C. Pfleiderer, Spontaneous skyrmion ground states in magneticmetals, Nature (London) **442**, 797 (2006).

[3] B. Binz, A. Vishwanath, and V. Aji, Theory of the Helical Spin Crystal: A Candidate for the Partially Ordered State of MnSi, Phys. Rev. Lett. **96**, 207202 (2006).

[4] S. Tewari, D. Belitz, and T. R. Kirkpatrick, Blue Quantum Fog: Chiral Condensation in Quantum Helimagnets, Phys. Rev. Lett. **96**, 047207 (2006).

[5] N. Nagaosa and Y. Tokura, Topological properties and dynamics of magnetic skyrmions, Nat. Nanotechnol. **8**, 899 (2013).

[6] R. Wiesendanger, Nanoscale magnetic skyrmions in metallic films and multilayers: A new twist for spintronics, Nat. Rev. Mater. **1**, 16044 (2016).

[7] A. Fert, N. Reyren, and V. Cros, Magnetic skyrmions: Advances in physics and potential applications, Nat. Rev. Mater. **2**, 17031 (2017).

[8] B. Göbel, I. Mertig, and O. A. Tretiakov, Beyond skyrmions: Review and perspectives of alternative magnetic quasiparticles, Phys. Rep. **895**, 1 (2021).

[9] I. Dzyaloshinsky, A thermodynamic theory of "weak" ferromagnetism of antiferromagnetics, J. Phys. Chem. Solids **4**, 241 (1958).

[10] T. Moriya, Anisotropic superexchange interaction and weak ferromagnetism, Phys. Rev. **120**, 91 (1960).

[11] S. Mülbauer, B. Binz, F. Jonietz, C. Pfleiderer, A. Rosch, A. Neubauer, R. Georgii, and P. Böni, Skyrmion lattice in a chiral magnet, Science **323**, 915 (2009).

[12] X. Z. Yu, Y. Onose, N. Kanazawa, J. H. Park, J. H. Han, Y. Matsui, N. Nagaosa, and Y. Tokura, Real-space observation of a two-dimensional skyrmion crystal, Nature (London) **465**, 901 (2010).

[13] S. Heinze, K. von Bergmann, M. Menzel, J. Brede, A. Kubetzka, R. Wiesendanger, G. Bihlmayer, and S. Blügel, Spontaneous atomic-scale magnetic skyrmion lattice in two dimensions, Nat. Phys. **7**, 713 (2011).

[14] W. Jiang, P. Upadhyaya, W. Zhang, G. Yu, M. B. Jungfleisch, F. Y. Fradin, J. E. Pearson, Y. Tserkovnyak, K. L. Wang, O. Heinonen *et al.*, Blowing magnetic skyrmion bubbles, Science **349**, 283 (2015).

[15] H. Y. Yuan and X. R. Wang, Skyrmion creation and manipulation by nano-second current pulses, Sci. Rep. **6**, 22638 (2016).

[16] N. E. Penthorn, X. Hao, Z. Wang, Y. Huai, and H. W. Jiang, Experimental Observation of Single Skyrmion Signatures in a Magnetic Tunnel Junction, Phys. Rev. Lett. **122**, 257201 (2019).

[17] L. Caretta, M. Mann, F. Büttner, K. Ueda, B. Pfau, C. M. Günther, P. Hessing, A. Churikova, C. Klose, M. Schneider *et al.*, Fast current-driven domain walls and small skyrmions in a compensated ferrimagnet, Nat. Nanotechnol. **13**, 1154 (2018).

[18] Y. Hirata, D.-H. Kim, S. K. Kim, D.-K. Lee, S.-H. Oh, D.-Y. Kim, T. Nishimura, T. Okuno, Y. Futakawa, and H. Yoshikawa, Vanishing skyrmion Hall effect at the angular momentum compensation temperature of a ferrimagnet, Nat. Nanotechnol. **14**, 232 (2019).

[19] H. Wu, F. Groß, B. Dai, D. Lujan, S. A. Razavi, P. Zhang, Y. Liu, K. Sobotkiewich, J. Förster, M. Weigand *et al.*, Ferrimagnetic skyrmions in topological insulator/ferrimagnet heterostructures, Adv. Mater. **32**, 2003380 (2020).

[20] T. Dohi, S. DuttaGupta, S. Fukami, and H. Ohno, Formation and current-induced motion of synthetic antiferromagnetic skyrmion bubbles, Nat. Commun. **10**, 5153 (2019).

[21] W. Legrand, D. Maccariello, F. Ajejas, S. Collin, A. Vecchiola, K. Bouzehouane, N. Reyren, V. Cros, and A. Fert, Room-temperature stabilization of antiferromagnetic skyrmions in synthetic antiferromagnets, Nat. Mater. **19**, 34 (2020).

[22] S. Gao, H. D. Rosales, F. A. G. Albarracín, V. Tsurkan, G. Kaur, T. Fennell, P. Steffens, M. Boehm, P. Čermák, A. Schneidewind *et al.*, Fractional antiferromagnetic skyrmion lattice induced by anisotropic couplings, Nature (London) **586**, 37 (2020).

[23] R. Chen, Y. Gao, X. Zhang, R. Zhang, S. Yin, X. Chen, X. Zhou, Y. Zhou, J. Xia, Y. Zhou *et al.*, Realization of isolated and high-density skyrmions at room temperature in uncompensated synthetic antiferromagnets, Nano Lett. **20**, 3299 (2020).

[24] J. Zang, M. Mostovoy, J. H. Han, and N. Nagaosa, Dynamics of Skyrmion Crystals in Metallic Thin Films, Phys. Rev. Lett. **107**, 136804 (2011).

[25] W. Jiang, X. Zhang, G. Yu, W. Zhang, X. Wang, M. B. Jungfleisch, J. E. Pearson, X. Cheng, O. Heinonen, K. L. Wang *et al.*, Direct observation of the skyrmion Hall effect, Nat. Phys. **13**, 162 (2017).

[26] J. Barker and O. A. Tretiakov, Static and Dynamical Properties of Antiferromagnetic Skyrmions in the Presence of Applied Current and Temperature, Phys. Rev. Lett. **116**, 147203 (2016).

[27] D. Bossini, S. Dal Conte, Y. Hashimoto, A. Secchi, R. V. Pisarev, T. Rasing, G. Cerullo, and A. V. Kimel, Macrospin dynamics in antiferromagnets triggered by sub-20 femtosecond injection of nanomagnons, Nat. Commun. **7**, 10645 (2016).

[28] P. E. Roy, R. M. Otxoa, and J. Wunderlich, Robust picosecond writing of a layered antiferromagnet by staggered spin-orbit fields, Phys. Rev. B **94**, 014439 (2016).

[29] K. Olejník, T. Seifert, Z. Kašpar, V. Novák, P. Wadley, R. P. Campion, M. Baumgartner, P. Gambardella, P. Němec, J. Wunderlich *et al.*, Terahertz electrical writing speed in an antiferromagnetic memory, Sci. Adv. **4**, eaar3566 (2018).

[30] F. Keffer and C. Kittel, Theory of antiferromagnetic resonance, Phys. Rev. **85**, 329 (1952).

[31] S.-W. Cheong, M. Fiebig, W. Wu, L. Chapon, and V. Kiryukhin, Seeing is believing: Visualization of antiferromagnetic domains, npj Quantum Mater. **5**, 3 (2020).

[32] K. G. Rana, R. L. Seeger, S. Ruiz-Gómez, R. Juge, Q. Zhang, V. T. Pham, M. Belmeguenai, S. Auffret, M. Foerster, and L. Aballe, Room temperature skyrmions in an exchange biased antiferromagnet, arXiv:2009.14796.

[33] X. Zhang, Y. Zhou, and M. Ezawa, Antiferromagnetic skyrmion: Stability, creation and manipulation, Sci. Rep. **6**, 24795 (2016).

[34] H. Yang, C. Wang, X. Wang, X. S. Wang, Y. Cao, and P. Yan, Twisted skyrmions at domain boundaries and the method of image skyrmions, Phys. Rev. B **98**, 014433 (2018).

[35] A. Salimath, F. Zhuo, R. Tomasello, G. Finocchio, and A. Manchon, Controlling the deformation of antiferromagnetic skyrmions in the high-velocity regime, Phys. Rev. B **101**, 024429 (2020).

[36] S. Zhou, C. Zheng, X. Chen, and Y. Liu, Skyrmion-based spin-torque nano-oscillator in synthetic antiferromagnetic nanodisks, J. Appl. Phys. **128**, 033907 (2020).

[37] H. Velkov, O. Gomonay, M. Beens, G. Schwiete, A. Brataas, J. Sinova, and R. A. Duine, Phenomenology of current-induced skyrmion motion in antiferromagnets, New J. Phys. **18**, 075016 (2016).

[38] H. Yang, C. Wang, T. Yu, Y. Cao, and P. Yan, Antiferromagnetism Emerging in a Ferromagnet with Gain, Phys. Rev. Lett. **121**, 197201 (2018).

[39] S. A. Díaz, J. Klinovaja, and D. Loss, Topological Magnons and Edge States in Antiferromagnetic Skyrmion Crystals, Phys. Rev. Lett. **122**, 187203 (2019).

[40] R. L. Silva, R. C. Silva, A. R. Pereira, and W. A. Moura-Melo, Antiferromagnetic skyrmions overcoming obstacles in a racetrack, J. Phys.: Condens Matter **31**, 225802 (2019).

[41] X. Liang, G. Zhao, L. Shen, J. Xia, L. Zhao, X. Zhang, and Y. Zhou, Dynamics of an antiferromagnetic skyrmion in a racetrack with a defect, Phys. Rev. B **100**, 144439 (2019).

[42] Z. Jin, T. T. Liu, W. H. Li, X. M. Zhang, Z. P. Hou, D. Y. Chen, Z. Fan, M. Zeng, X. B. Lu *et al.*, Dynamics of antiferromagnetic skyrmions in the absence or presence of pinning defects, Phys. Rev. B **102**, 054419 (2020).

[43] H. Min, R. D. McMichael, M. J. Donahue, J. Miltat, and M. D. Stiles, Effects of Disorder and Internal Dynamics on Vortex Wall Propagation, Phys. Rev. Lett. **104**, 217201 (2010).

[44] H. Y. Yuan and X. R. Wang, Domain wall pinning in notched nanowires, Phys. Rev. B **89**, 054423 (2014).

[45] T. Klein, R. Marlaud, C. Marcenat, H. Cercellier, M. Konczykowski, C. J. van der Beek, V. Mosser, H. S. Lee, and S. I. Lee, First-Order Transition in the Magnetic Vortex Matter in Superconducting MgB_2 Tuned by Disorder, Phys. Rev. Lett. **105**, 047001 (2010).

[46] J.-V. Kim and M.-W. Yoo, Current-driven skyrmion dynamics in disordered films, Appl. Phys. Lett. **110**, 132404 (2017).

[47] X. Gong, H. Y. Yuan, and X. R. Wang, Current-driven skyrmion motion in granular films, Phys. Rev. B **101**, 064421 (2020).

[48] L. Xiong, B. Zheng, M. H. Jin, and N. J. Zhou, Anisotropic critical behavior of current-driven skyrmion dynamics in chiral magnets with disorder, New J. Phys. **22**, 033043 (2020).

[49] A. A. Thiele, Steady-State Motion of Magnetic Domains, Phys. Rev. Lett. **30**, 230 (1973).

[50] H. Y. Yuan, Q. Liu, K. Xia, Z. Yuan, and X. R. Wang, Proper dissipative torques in antiferromagnetic dynamics, Europhys. Lett. **126**, 67006 (2010).

[51] S. Zhang and Z. Li, Roles of Nonequilibrium Conduction Electrons on the Magnetization Dynamics of Ferromagnets, Phys. Rev. Lett. **93**, 127204 (2004).

[52] A. Vansteenkiste, J. Leliaert, M. Dvornik, M. Helsen, F. Garcia Sanchez, and B. Van Waeyenberge, The design and verification of MuMax3, AIP Adv. **4**, 107133 (2014).

[53] S. Havlin and D. ben-Avraham, Diffusion in disordered media, Adv. Phys. **51**, 187 (2002).

[54] J. Zázvorka, F. Jakobs, D. Heinze, N. Keil, S. Kromin, S. Jaiswal, K. Litzius, G. Jakob, P. Virnau, and D. Pinna, Thermal skyrmion diffusion used in a reshuffler device, Nat. Nanotechnol. **14**, 658 (2019).

[55] L. Zhao, Z. Wang, X. Zhang, X. Liang, J. Xia, K. Wu, H.-A. Zhou, Y. Dong, G. Yu, K. L. Wang *et al.*, Topology-Dependent Brownian Gyromotion of a Single Skyrmion, Phys. Rev. Lett. **125**, 027206 (2020).

[56] W. F. Brown, Jr., Thermal fluctuations of a single-domain particle, Phys. Rev. **130**, 1677 (1963).

[57] E. M. Lifshitz and L. P. Pitaevskii, *Statistical Physics (Part 2): Theory of the Condensed State, Course of Theoretical Physics* (Pergamon Press, Oxford, 1980), Vol. 9.

[58] E. G. Tveten, A. Qaiumzadeh, O. A. Tretiakov, and A. Brataas, Staggered Dynamics in Antiferromagnets by Collective Coordinates, Phys. Rev. Lett. **110**, 127208 (2013).

[59] X. S. Wang, H. Y. Yuan, and X. R. Wang, A theory on skyrmion size, Commun. Phys **1**, 31 (2018).

[60] P. B. Ndiaye, C. A. Akosa, and A. Manchon, Topological Hall and spin Hall effects in disordered skyrmionic textures, Phys. Rev. B **95**, 064426 (2017).

[61] R. K. Pathria and P. D. Beale, *Statistical Mechanics*, 3rd ed. (Academic Press, San Diego, 2011), Chap. 15.